ELSEVIER

Journal of Nuclear Materials 240 (1997) 83–99

journal of nuclear materials

Interpretation of Inconel 600 behavior in the active region in tritiated water containing chloride–fluoride ions between pH 1 and 3.5

G. Bellanger [a,*], J.J. Rameau [b]

[a] Commissariat à l'Energie Atomique, Centre d'Etudes de Valduc, F-21120 Is sur Tille, France
[b] Centre de Recherche en Electrochimie Minérale et Génie des Procédés, Ecole Nationale Supérieure d'Electrochimie et d'Electrometallurgie / Institut National Polytechnique de Grenoble, Domaine Universitaire, B.P. 75, F-38402 Saint Martin d'Hères, France

Received 29 January 1996; accepted 25 September 1996

Abstract

Voltammetric and impedance measurements were carried out to study the corrosion behavior of Inconel 600, a candidate material for radioactive plants using acid tritiated water solutions containing Cl^- and F^- ions. The polarization and voltammetric curves show the localized corrosion region over a wide range of potentials going from the corrosion potential up to the passivity and transpassivity. This indicates that the localized corrosion occurs in the active potentials. The voltammetric curves and electrochemical impedance diagrams show the effect of potential, pH, Cl^-, and F^- concentrations on Inconel 600 behavior in the overlapping active and localized corrosion regions. These indicate that there are definitely reactions with the oxide layer and that there are several processes occurring simultaneously: adsorption of Cl^- and F^-, localized and active corrosion, oxide layer dissolution and ionic diffusion. The experimental data and simulated spectra were fitted by equivalent circuits and the component values were determined.

1. Introduction

Nickel-based alloys are extensively used in the nuclear industry for their corrosion resistance. Most frequently, the localized corrosion resistance is the reason for this choice. Nevertheless, all nickel-based alloys are not equivalent and to avoid inopportune problems there must be a judicious selection founded on accurate knowledge of the medium and alloy characteristics. Among these alloys, the Inconel 600, 690 and X-750 can be positioned in the same family. This study concerns localized corrosion in the active region of Inconel 600 (UNS N06600) for nuclear reprocessing installations using highly radioactive aqueous solutions, specifically involving tritiated water. Tritium decays by emission of a β^- particle and a ν_e antineutrino. The energy released decomposes water molecules with the production of significant concentrations of radiolytic hydrogen peroxide and dissolved oxygen, particularly if the tritiated water is concentrated and stored for long periods in closed containers:

$$^3H_2O \rightarrow 2\,^3He + O + 2\beta^- + \nu_e \quad E_{max} = 18.6 \times 2\ \text{keV}, \tag{1}$$

$$2\,^3H_2O + \beta^- \rightarrow {}^3H^\cdot + {}^3HO_2^\cdot + {}^3HO_2^- \ldots \rightarrow {}^3H_2O_2 + 2\,^3H^+. \tag{2}$$

The effect of the β^- particles and the action of the hydrogen peroxide on the passive oxide layers have been reported previously [1,2]. Stress corrosion cracking by tritium in steels was studied by Chêne et al. [3,4] and in our laboratories [5,6]. In tritiated water, a high radiolytic gas pressure leads to more positive values for the corrosion potential and free potential. An acidic medium was selected since relatively concentrated acid solutions are produced in tritiated water reprocessing installations during

* Corresponding author.

PII S0022-3115(96)00673-3

catalytic gaseous tritium oxidation cycles at 450°C with air and finely divided palladium. The acidification is explained by the effect of β^- particles on the nitrogen in the air, the reactions are, from Bruggeman et al [7], Burns and Moore [8], Linacre and Marsh [9], Wright et al. [10].

$$N_2 + \beta^- \rightarrow 2N\,. \tag{3}$$

$$N + 3^3HO_2^- \rightarrow {}^3HNO_3 + {}^3H_2O + 2O\,. \tag{4}$$

The $^3HO_2^-$ radical is an intermediate species produced in water autoradiolysis. Thus, the final products from the catalytic oxidation cycles give an appreciable $^3H^+$ concentration. As with water, the β^- particle energy decomposes organic polymer joints in valves or vacuum pump oils when these are in contact with gaseous tritium or tritiated water. If these polymers have R–F or R–Cl bonds, the decomposition reactions in acid media are

$$R\text{–}F + \beta^- \rightarrow F^- + CO_2 + R'\text{–}\,. \tag{5}$$

$$R\text{–}Cl + \beta^- \rightarrow Cl^- + CO_2 + R'\text{–}\,. \tag{6}$$

It has been observed that the decomposition of sintered Ni + PTFE or PVC composites tested in our laboratories is visible after two months and the concentrated tritiated water used (i.e., 10 TBq cm^{-3}) becomes brownish during the decomposition. If the PTFE or PVC is subsequently removed from the tritiated water, the solution becomes colorless. The products formed have been 'digested' by the tritiated water. This contains an appreciable concentration of Cl^- and F^- (5×10^{-2} mol dm^{-3}). Consequently, the effects of F^- and Cl^- ions at acid pH were studied, first separately, then together keeping a constant Cl^- concentration and controlling the pH and fluoride concentration for the range of localized corrosion potentials in the anodic peak of the active region.

2. Experimental equipment

The tritium concentration in tritiated water was determined using a Kontron SL4000 liquid scintillation spectrophotometer as well as a Cetaram RT64 microcalorimeter. The electrochemical equipment consisted of a Tacussel bipotentiostat and triangular signal generator (PRT-20 and GSTP3) connected to a Tektronix 2230 digital oscilloscope to display the currents obtained at high scan rates in cyclic voltammetry. After storage in the oscilloscope, the curves were recorded on a Hewlett-Packard AXY HP 7440 plotter. The electrochemical impedance diagrams were obtained with a Tacussel ZCP 130 T generator controlled by a Hewlett-Packard 486 micro-computer monitored by a HP 82324 coprocessor. To analyze the electrochemical processes thoroughly, it is necessary to measure the impedance over a large frequency range. Thus, the frequency scans were made starting from 10^5 Hz, down to 10^{-2} Hz with a sinusoidal amplitude of 5 mV and five steps per decade. The spectra were judged to be satisfactory when two tests were identical over the whole frequency range. The Circelec simulation computer program, written by Diard et al. [11,12], was used to interpret the experimental spectra, making it possible to obtain values of the equivalent circuit elements at the electrode surface. The reference and auxiliary electrodes were, respectively, saturated calomel (SCE) and platinum electrodes. A platinum wire was connected to the reference electrode through a 0.1 μF capacitor to eliminate any possible capacitive interferences and short connection leads were used to minimize inductance effects. The standard configuration Inconel 600 disk electrode was made by the Tacussel firm. The electrode consisted of an Inconel 600 rod well embedded in a Teflon cylindrical tube to avoid electrolyte infiltration which would modify the curve shape. Its rotation rate was determined in each test. The composition of nickel-base Inconel 600 is given in Table 1. Nickel has a positive effect with respect to pitting, cavern and cracking corrosion, and it provides better pitting behavior than iron. According to Rouby [13], Houlle [14] and Duporton and Vernaux [15], copper improves resistance to pitting and crevice corrosion by displacing the pitting corrosion potential to higher values. Chromium increases the passivity domain by forming a mixed passive oxide layer. Titanium and aluminum are essential for precipitation in the alloy contributing to less pitting and intergranular corrosion. Titanium reacts easily with carbon forming titanium carbides avoiding the depletion in chromium around the grain boundaries. Although Inconel 600 contains titanium, this alloy is liable to undergo intergranular attack in circumstances similar to those of stainless steels. This attack is linked to chromium depletion around the grain boundary following the formation of chromium-rich carbides. This local chromium depletion is such that its concentration is below the stable passivity threshold. The solutions proposed are identical to those recommended for the stainless steels:

- limit the carbon concentration to a low level to prevent chromium carbide formation,
- add elements in order to form more stable carbides than $Cr_{23}C_6$ in grain boundaries.

The silicon is due to the fact that it could not be avoided or it is added to improve the corrosion resistance in an oxidizing medium used at high temperatures when its concentration is appreciable (0.8–2 wt%). From visual examinations by a Cambridge S90 scanning electron microscope, the microstructure of the Inconel 600 electropolished was characterized by grain sizes between 5 and 20

Table 1
Inconel 600 composition

	Element								
	Cr	Fe	C	Mn	Si	Cu	Al	Ti	Ni
Wt%	16	8.7	0.04	0.2	0.2	0.2	0.2	0.2	bal.

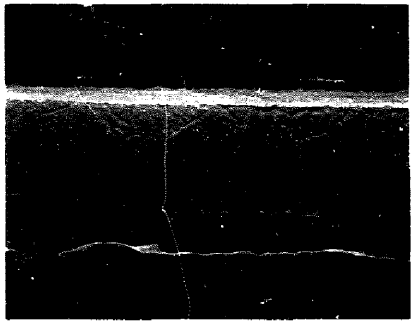

Fig. 1. Scanning electron microscopy photograph of electropolished Inconel 600 showing grains (roughly 5–20 diameter).

μm (Fig. 1). Inconel 600 was heat treated at 1150°C and rapidly air cooled (hypertrempe) in order to homogenize the face cubic centered austenitic structure.

The electrolyte contained F^-, Cl^- and $^3H^+$ ions and their concentrations were measured with specific electrodes in order to determine their respective effects on Inconel 600 behavior. Prior to each use, the disk electrode was mechanically polished on 2000 mesh grade silicon carbide sheets, then with diamond paste down to 1 μm and washed with deionized water. The roughness factor for polished Inconel 600 is estimated to be in the range 1–1.2 from Schulze and Macagno [16] and Kerrec et al. [17]. In this way, the electrode acquired a reproducible silvery bright surface. The impedance measurements were made in the ac mode, after immersion in the electrolyte deaerated by bubbling nitrogen for 10 min. pH was measured using a Tacussel Minisis 5000 pH meter taking into account the difference between the pK (dissociation constant) of light and tritiated water ($pK^3_{H_2O} = 15.21$) to calibrate the pH meter.

3. Experimental results

To suppress any uncertainties, the study was carried out after decomposition of the radiolytic hydrogen peroxide and dissolved oxygen at −1.1 V/SCE according to our previous study [18]. The tritium concentration was kept constant (10 TBq cm^{-3}), to ensure that there was no variation in the amount of radiation energy arriving at the oxide layer.

3.1. Cyclic voltammetry

3.1.1. Voltammograms obtained with chloride present

The use of relatively fast scan rates is unusual in corrosion testing, and the justification for this technique is given by Morris and Scarberry [19]. With rapid-scan curves it is easier to reveal peaks where inflections in the slow-scan curves suggest they might exist. The experimental voltammograms given in Fig. 2 were obtained for Inconel 600 and with chloride concentration kept constant at 5×10^{-2} mol dm^{-3} while the pH varied between 1 and 3.5 (curves 2 to 5). For comparison, a curve was also drawn without chloride (curve 1). In this curve, the active peak is seen at 0.2 V/SCE and the passive region extends from 0.2 to 0.8 V/SCE. When the potential sweep is reversed at 1 V/SCE, the presence of a cathodic peak shows that the passive oxide layer can be reduced to around −0.5 V/SCE. The large potential difference between cathodic and anodic peaks signifies that the passive oxide is difficult to reduce. In curves 2 to 5 obtained with Cl^-, the anodic peak is observed in the localized corrosion current, which increases at lower pH, and continues to be produced during the backward scan to reach the corrosion products reduction peak, whose height slightly decreases with increasing pH. In the forward and backward scans, the respective different currents depend on pH. In these curves, the difference between anodic and cathodic charges is greater than that in curve 1. This difference is not due to any difficulty in reducing the passive oxide layer under the localized corrosion conditions, since it does not form. Stirring would contribute to sweeping away corrosion products from the electrolyte–oxide interface [20]. Consequently, an anodic reaction accompanied by ionic diffusion

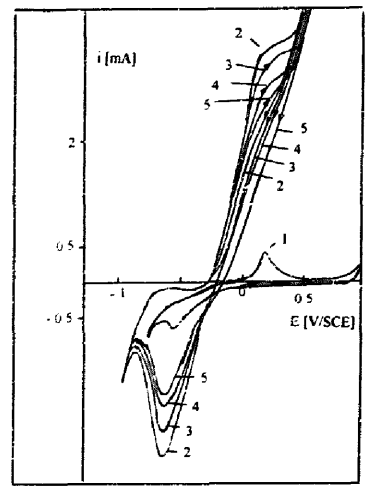

Fig. 2. Voltammetric curves of Inconel 600 surface area: 0.2 cm^2, temperature: 20°C, scan rate: 0.2 V s^{-1}, ω: 2000 rpm, curve (1): polished Inconel 600, without Cl^-, pH 2, curves (2) to (5): with Cl^-: 5×10^{-2} mol dm^{-3}, (2): pH 1, (3): pH 2, (4): pH 2.7, (5): pH 3.5.

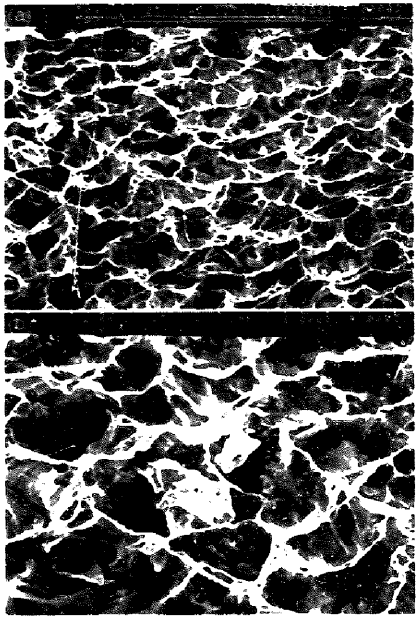

Fig. 3. SEM photograph of Inconel 600 showing numerous cavities as widespread pits. (a): magnification of 504, (b): magnification of 1060. E: 0.1 V/SCE, C_F: 5×10^{-2} mol dm^{-3}, pH 3.5.

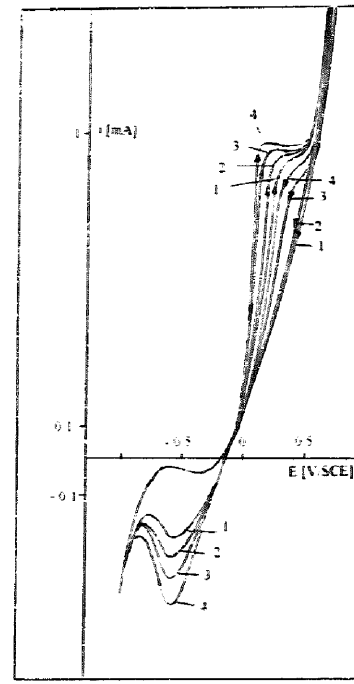

Fig. 4. Voltammetric curves of Inconel 600 surface area: 0.2 cm^2, temperature: 20°C, scan rate: 0.2 V s^{-1}, ω 2000 rpm, effect of fluoride: (1) 10^{-2} mol dm^{-3}, pH 1, (2): 6×10^{-2} mol dm^{-3}, pH 1.9, (3): 8×10^{-2} mol dm^{-3}, pH 2.3, (4): 0.1 mol dm^{-3}, pH 3.5.

would occur in the oxide layer. After these results were obtained by voltammetry, the alloy surface was examined by scanning electron microscopy (SEM) by applying a potential in the active peak. The surface aspect is shown in Fig. 3. Note that shallow, broad and numerous cavities as widespread pits, about 10 μm diameter, and some crusts are visible at this surface and correspond to localized corrosion in the active region as shown by voltammetry.

3.1.2. Voltammograms obtained with fluoride present

The effect of fluoride and pH variations on localized corrosion currents are given in Fig. 4. In these curves, pH increases with the selected fluoride concentrations between 10^{-2} and 0.1 mol dm^{-3}, to reach pH 3.5 (Table 2) corresponding to the pK_a of the fluoride–hydrofluoric acid buffer. In contrast to chloride, the anodic currents are higher when the pH increases; this results from the fluoride concentration increase with pH. As with chlorides, the anodic peak is observed in the localized corrosion region. In the backward scan, the corrosion products reduction peak current increases with fluoride concentration like that in the anodic peak. SEM examinations were carried out at the active-localized corrosion potentials. The Inconel 600 surface appearance on applying a potential of 0.1 V/SCE is shown in Fig. 5. Some pits and microcracking are observed, which result from fluoride ions at acid pH. Microcracking and pits would be induced by $^3H^+$ reduction with formation of gaseous hydrogen isotopes in tips of pits and in grain boundaries (Fig. 6) for the active region; these lead to embrittlement as shown by Wieckowski et al. [21] and Ford et al. [22] in radioactive media. To explain this attack, Pickering et al. [23] show that hydrogen is generated within the grain boundary even though the alloy surface is about 200 mV more noble than the equilibrium

Table 2
Effect of F$^-$ on pH

	F$^-$ (mol dm^{-3})					
	10^{-2}	4×10^{-2}	6×10^{-2}	8×10^{-2}	9×10^{-2}	10^{-1}
pH	1	1.3	1.9	2.3	3.1	3.5

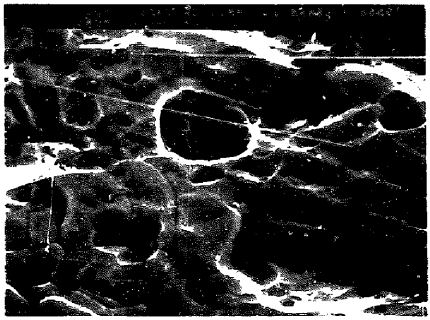

Fig. 5. SEM photograph of Inconel 600. E: 0.1 V/SCE, F^-: 0.1 mol dm^{-3}, pH 3.5.

potential of the hydrogen evolution reaction in the bulk electrolyte. As indicated by Ballinger et al. [24], the near grain boundary chromium concentration of Inconel 600 exhibits a degree of variability but in general is lower with respect to the matrix and the grain boundary. Pinard-Legry et al. [25] showed that the intergranular microcracking linked to hydride formation obtained by electrolysis is observed on Inconel 600. As in the ferritic steels, hydrogen preferentially accumulates and diffuses in the perturbed regions such as the carbide-grain boundary interfaces leading to intergranular corrosion. To show the morphology of the microcracking induced directly by tritium, the surface of Inconel 600 was examined by SEM. Figs. 1 and 7 show the cross-sectional photographs of two Inconel 600 membranes, one without (Fig. 1) and the other charged with tritium (Fig. 7(a), (b)). Without tritium charging, there is no loosening along grain boundaries. The intergranular grooves in Fig. 7(a) obtained after tritium charging are clearly more visible in-depth, which shows deeper localized corrosion by stress cracking of grain boundaries induced by tritium diffusion and absorption. Small cavities, about 0.2 μm diameter, are evident within the grains, with their population density dependent on the particular grain

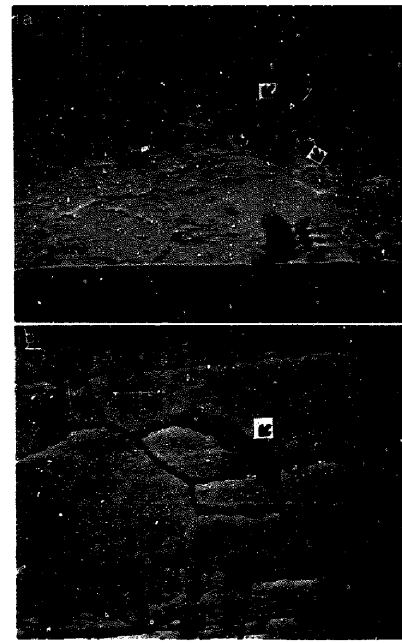

Fig. 7. Scanning electron microscopy. Localized corrosion in grain boundaries induced by tritium in cross-section of Inconel 600 membrane. (a): arrows showing grain boundary loosening and highly localized grain attack. (b): detail of photograph (a) showing broader attack of the intergranular groove by tritium diffusion (arrow).

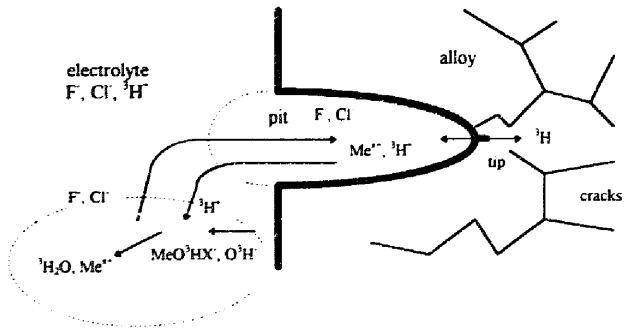

Fig. 6. Schematic of various species in pits associated with tritium embrittlement in aqueous environment. X^- represents Cl^- and F^-.

selected. Furthermore, cavities are preferentially located adjacent to the grain boundaries. They can correspond to heterogeneities, for example, carbide precipitates, most probably Cr-rich carbides, depleted around, and inside the grains. More detailed examination on photograph (b) (Fig. 7) shows that locally there is a broader attack of the intergranular groove in some grain boundaries. This must be due to weakening of the boundary by preferential tritium diffusion. From these examinations of the Inconel 600 and discussions in the literature, it is clear that tritium penetrates Inconel 600 by grain boundaries inducing intergranular microcracking. Thus SEM examinations in Fig. 5, support the formation of localized corrosion and cracks under these conditions.

3.1.3. Voltammograms obtained with chloride and fluoride present

3.1.3.1. Fluoride and pH effects. These specific cases of localized corrosion by Cl^- or F^- with two converse behaviors for the same pH variation will help understanding the change in the voltammograms for a H^+, Cl^- and F^- mixture where Cl^- is kept constant (5×10.2 mol dm^{-3}) while F^- varies (10^{-2} to 0.1 mol dm^{-3}) with pH up to the value of pK_a, i.e., 3.5. In Fig. 8(a), the anodic peak decreases then increases when the F^- concentration and pH increase. This suggests first, that there are two influences: a slight limitation of Inconel 600 localized corrosion due to the fact that the pH increases and the F^-

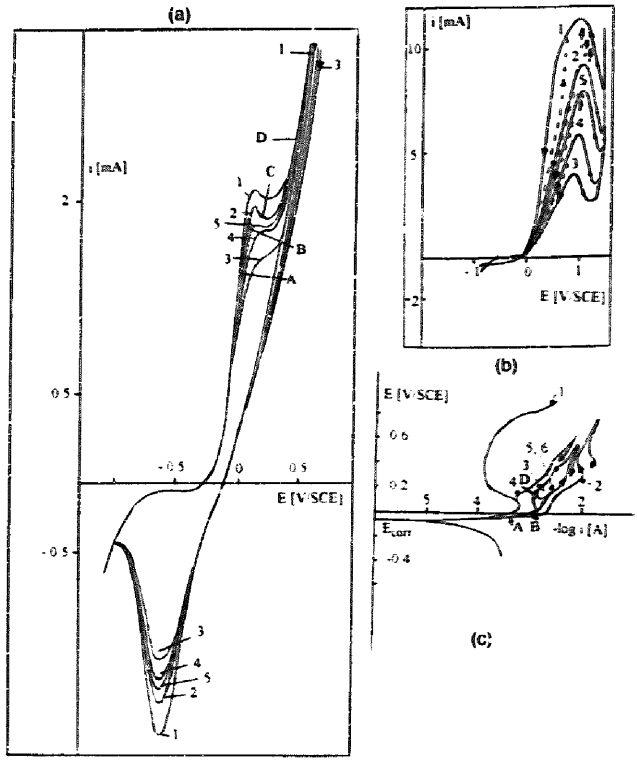

Fig. 8. Voltammetric and polarization curves of Inconel 600 (a, b): voltammetric curves: surface area: 0.2 cm^2, temperature: 20°C, scan rate: 0.2 V s^{-1}, ω: 2000 rpm, Cl^-: 5×10^{-2} mol dm^{-3}, effect of fluoride and pH: (1): 10^{-2} mol dm^{-3}, pH 1, (2): 6×10^{-2} mol dm^{-3}, pH 2.3, (3): 8×10^{-2} mol dm^{-3}, pH 2.9, (4): 0.1 mol dm^{-3}, pH 3.5, (5): 0.12 mol dm^{-3}, pH 3.6, - - - forward scan, ——— backward scan. (c): polarization curves: surface area: 0.2 cm^2, temperature: 20°C, scan rate: 5 mV s^{-1}, ω: 2000 rpm, initial pH: 1, effect of fluoride and pH: curve (1): pH 1, without Cl^- and F^-, curves (2) to (6): with 5×10^{-2} mol dm^{-3} Cl^-, (2): 10^{-2} mol dm^{-3} F^-, pH 1, (3): 6×10^{-2} mol dm^{-3} F^-, pH 2.3, (4): 8×10^{-2} mol dm^{-3} F^-, pH 2.9, (5): 0.1 mol dm^{-3} F^-, pH 3.5, (6): 0.12 mol dm^{-3} F^-, pH 3.6.

and Cl^- concentrations must be high enough to produce more localized corrosion. In addition, the gradual increase then decrease of localized corrosion current, as the fluoride concentration increases, corresponds to the same variation of the cathodic peak (−0.5 V/SCE) attributed to the reduction of corrosion products. This experimental observation also clearly indicates that the electrode process is controlled by the surface mechanisms. In second measurements, the effects of fluoride and pH are seen in the voltammograms realized at a higher current scale in order to obtain better observation of pitting currents in the passive and transpassive regions (Fig. 8(b)). Before the reversal scan, the pitting current obtained with chloride decreases then increases when fluoride concentration increases showing an unusual hysteresis shape in the presence of pitting. The fluoride ions are expected to form products adsorbed on the oxide layer that initiate pitting with respect to pH like chloride ions in agreement with the reaction given by Farvaque-Béra and Leistikow [26]:

$$Me(O^3H)_2 + X^- \rightarrow MeO^3HX_{ads} + O^3H^-. \quad (7)$$

where X^- is Cl^- or F^- and Me represents Inconel 600. Increasing pH and F^- concentration may modify the surface by two ways; this could be examined later by scanning electron microscopy and impedance spectroscopy.

To facilitate the selection of the anodic peak potentials for obtaining impedance diagrams, polarization curves were plotted using a lower scan rate (Fig. 8(c)) and for the same F^-, Cl^- concentrations and pH (curves 2 to 6) as those in Fig. 8(a), (b), and also without Cl^- and F^- (Fig. 8, curve 1). These curves can be used to justify earlier statements. The anodic peak is found more precisely at 0.05 V/SCE, and the slight difference with voltammograms would appear to result from the scan rates, therefore due to reaction kinetics. In these curves, a high localized corrosion current is maintained even at a low scan rate. At low scan rates, chloride and fluoride are more easily adsorbed and subsequently diffuse in the oxide layer leading to localized corrosion in conformity with adsorption and diffusion kinetics. In the anodic peak and pitting region, it is seen that the current decreases, then increases when the F^- concentration and pH increase; the interpretation is the same as that given for the voltammograms (Fig. 8(a), (b)). It can be seen that the corrosion potential ($E_{corr} = -0.075$ V/SCE) is the same at different F^- concentrations. Polarization curves (Fig. 8) show a well defined localized corrosion region over a wide range of potentials going from the corrosion potential up to the transpassivity in the forward scan. The repassivity potential in the backward scan is near the corrosion potential. This indicates a corrosion risk by crevices with pitting.

3.1.3.2. Effect of varying stirring and scan rate. In Fig. 9, stirring increases the anodic peak and shifts the negative current in the shoulder toward positive values, whereas the

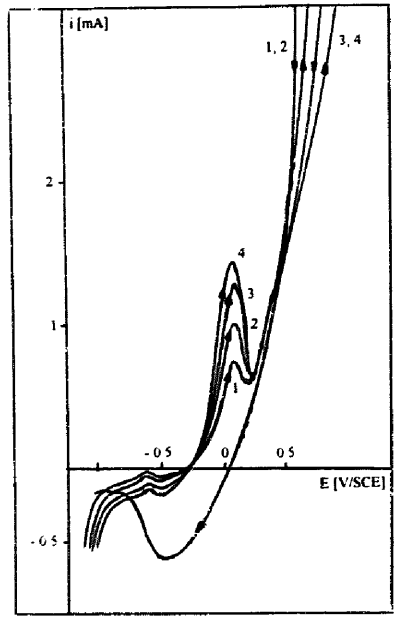

Fig. 9. Voltammetric curves of Inconel 600 surface area: 0.2 cm^2, temperature: 20°C, Cl^-: 5×10^{-2} mol dm^{-3}, F^-: 5×10^{-2} mol dm^{-3}, pH 1.7, scan rate: 20 mV s^{-1}, ω: (1): 500, (2): 1000, (3): 2000, (4): 3000 rpm.

corrosion product reduction peak does not change indicating that a superficial oxide layer would favor crevice corrosion. Evidently the anodic peak is affected by active behavior, and the cathodic peak is essentially related to the oxide layer. Plotting the anodic peak current versus stirring, a straight line is obtained which fits the Levich equation:

$$i_p = 1.24FD^{2/3}\Upsilon^{-1/6}v^{0.5}A\omega^{0.5}C_{sp}. \quad (8)$$

where v is the scan rate, ω is the electrode rotation rate, D is the diffusion coefficient, A is electrode surface, Υ is the dynamic viscosity, F is Faraday's constant and C_{sp} is the species concentration. An experimental value for the diffusion coefficient of 5×10^{-5} cm^2 s^{-1} is then found. This value would depend in particular on the absence or the presence of oxide, but it is close to the usual values obtained for aqueous media [27]. The integrated charge (Q_c) for the cathodic peak is higher than those (Q_a) obtained for the active peak and the ratio, Q_c/Q_a decreases when the stirring increases. As the volume of tritiated water is small, it is also deduced that a few species would be trapped below the surface oxide layer and could

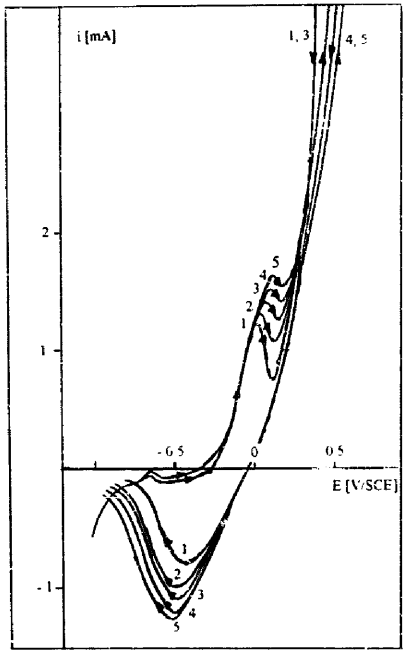

Fig. 10. Voltammetric curves of Inconel 600 surface area: 0.2 cm^2, temperature: 20°C, ω: 2000 rpm, Cl^-: 5×10^{-2} mol dm^{-3}, F^-: 5×10^{-2} mol dm^{-3}, pH 1.7, t: (1): 20, (2): 40, (3): 60, (4): 80, (5): 100 mV s^{-1}.

favor crevice corrosion. It can also be seen that the localized corrosion current varies in the opposite direction to that of the anodic peak with stirring. Adsorption of Cl^- and F^- followed by diffusion in the oxide layer by ionic vacancies or the O^{2-} lattice [28] would be slowed down due to the soluble hydroxide-Cl^-, F^- complex removed by stirring, which subsequently limits localized corrosion. Consequently, the localized corrosion rate is dependent on the intermediate species (e.g., MeO^3HX^-, local $^3H^+$) remaining at the surface of the Inconel 600, i.e., on the species kinetics. The soluble hydroxide-Cl^- or F^- complex formed locally dissolves the oxide layer up to the alloy which is corroded according to

$$Me + x^3H_2O \rightarrow Me(O^3H)_x + x^3H^+ + xe^- \quad (9)$$

This reaction leads to increasing the acidity in pits which dissolves the hydroxide and accelerates localized corrosion in absence of stirring.

In Fig. 10, the scan rate was varied from 20 to 100 mV s^{-1}. An increase in the scan rate leads to increasing anodic and cathodic peaks, decreasing pitting currents and does not significantly change the current in the shoulder which can be the result of adsorbed tritium.

With increasing scan rates, the two peaks are displaced in positive and negative potential directions, respectively. Plots of the logarithm of current in the anodic peak versus logarithm of scan rate give a straight line with a slope close to 0.5. Plots of peak current versus the square root of scan rate have also been performed. For the anodic peak, a good straight line was obtained; the slope is about 4.5 mA cm^{-2} $V^{-0.5}$ $s^{0.5}$ and corresponds to the value calculated from Delahay's equation for a reaction controlled by ionic diffusion [27]. Thus, these peaks correspond well to the classical faradaic and capacitance current equations given in voltammetry, i.e., an active behavior. The value calculated from the active peak is about 2.5 mC cm^{-2}, and consequently indicates the formation of a multi-oxide layer. Effectively, X-ray photoelectron spectroscopy examinations made by Moffat and Latanision [29] indicate that the monolayer equivaleat charge is about 0.6 mC cm^{-2}. In localized corrosion, at low scan rates, chloride and fluoride ions are more readily adsorbed and subsequently diffuse in the oxide layer following adsorption and diffusion kinetics. Local dissolution of the oxide layer by complex hydrox-

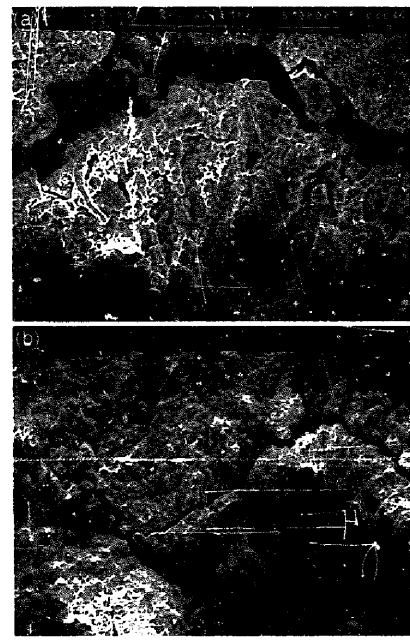

Fig. 11. SEM photograph of Inconel 600. E: 0.1 V/SCE, Cl^-: 5×10^{-2} mol dm^{-3}, F^-: 0.1 mol dm^{-3}, pH 3.5.

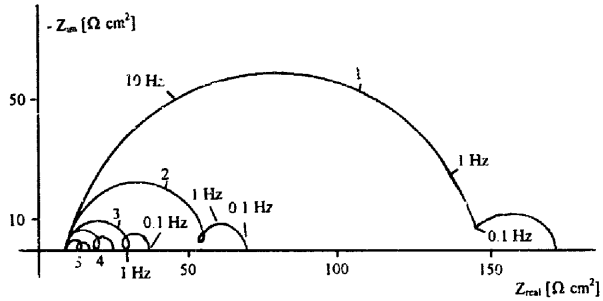

Fig. 12. Impedance diagrams of Inconel 600 surface area: 0.2 cm^2, temperature: 20°C, ω: 2000 rpm, pH: 1, Cl^-: 5×10^{-2} mol dm^{-3}, potential effect: (1): 0, (2): 0.025, (3): 0.065, (4) 0.08, (5): 0.1 V/SCE.

ide–chloride and fluoride and localized attack of the underlying alloy by acid formation are also involved here.

Interpretation of the previous voltammograms is not easy. On increasing the fluoride concentration in the presence of chloride, the pitting current should increase, and in fact, this decreases, then increases. These surprising results require SEM examinations. Inconel 600 potentiostated at 0.1 V/SCE shows localized corrosion in the active peak, with the formation of cracks or crevices as indicated by Pickering [30] and Cho and Pickering [31], and oxide crusts and grain decohesion of the oxide layer (Fig. 11) which can lead to porosity and the resulting ionic diffusion in the oxide layer, then sublayer corrosion. Finally, the results obtained by voltammetry and SEM examinations show that Inconel 600 is corroded at the same time by active corrosion and localized corrosion in the anodic peak.

3.2. Electrochemical impedance spectroscopy

3.2.1. Spectra obtained with chloride present

The impedance diagrams obtained with 5×10^{-2} mol dm^{-3} Cl^- are shown for different potentials (Fig. 12) in the overlapping active and localized corrosion regions, more exactly at the pitting beginning potentials, and different chloride concentrations between 5×10^{-3} and 5×10^{-2} mol dm^{-3} for pH 1 (Fig. 13). The diagrams show two capacitive semi-circles at high and low frequencies; these are separated by a loop for higher potentials or Cl^- concentrations. These semi-circles indicate two mechanisms as mentioned in Section 3.2.3.

The loop can be ascribed to adsorption phenomena. As shown in Figs. 12 and 13, each capacitive semi-circle decreases when the potentials are slightly shifted to more positive values or when the chloride concentration increases.

The impedance diagrams in Fig. 14 were obtained at different pH between 1 and 3.5, for a constant Cl^- concentration (5×10^{-2} mol dm^{-3}), and a potential located in the anodic peak. In these spectra, two capacitive semi-circles are obtained. Their size increases with pH, suggesting that corrosion decreases at higher pH. The capacitive semi-circle obtained at a low frequency can be followed or preceded by an inductive loop. Its origin is the same as that for Fig. 12.

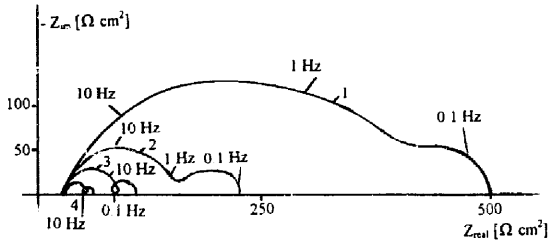

Fig. 13. Impedance diagrams of Inconel 600 surface area: 0.2 cm^2, temperature: 20°C, ω: 2000 rpm, pH: 1, E: 0.05 V/SCE, effect of Cl^-: (1): 5×10^{-3}, (2): 10^{-2}, (3): 2×10^{-2}, (4) 5×10^{-2} mol dm^{-3}.

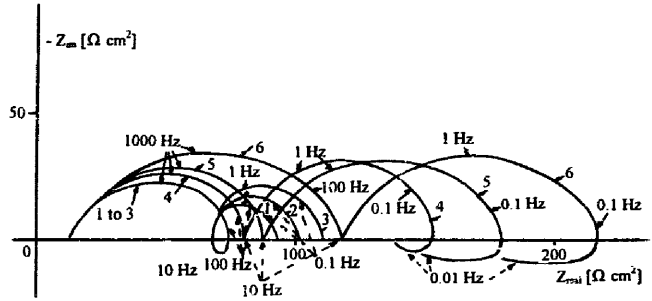

Fig. 14. Impedance diagrams of Inconel 600 surface area: 0.2 cm^2, temperature: 20°C, ω: 2000 rpm, E: 0.15 V/SCE, Cl^-: 5×10^{-2} mol dm^{-3}, effect of pH: (1): pH 1, (2): pH 1.5, (3): pH 2, (4): pH 3, (5): pH 3.5, (6): pH 4.

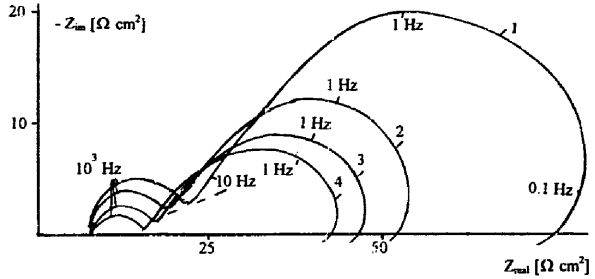

Fig. 15. Impedance diagrams of Inconel 600 surface area: 0.2 cm^2, temperature: 20°C, ω: 2000 rpm, E: 0.05 V/SCE, effect of F^-: (1): 10^{-2}, pH 1, (2): 6×10^{-2}, pH 1.9, (3): 8×10^{-2}, pH 2.3, (4): 10^{-1} mol dm^{-3}, pH 3.5.

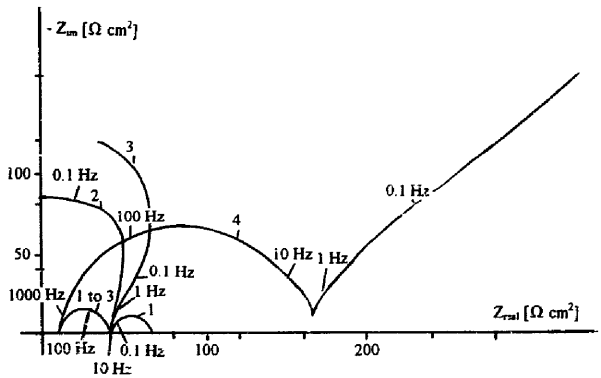

Fig. 16. Impedance diagrams of Inconel 600 surface area: 0.2 cm^2, temperature: 20°C, ω: 2000 rpm, Cl^-: 5×10^{-2} mol dm^{-3}, F^-: 5×10^{-2} mol dm^{-3}, pH 1.7, potential effect: (1): 0.03, (2): 0.05, (3): 0.07, (4): 0.1 V/SCE.

3.2.2. Spectra obtained with fluoride present

The impedance diagrams obtained with different fluoride concentrations between 10^{-2} and 0.1 mol dm^{-3} and for 0.05 V/SCE are shown in Fig. 15. At this potential chosen in the anodic peak, it is seen that the size of the two capacitive semi-circles decreases when the fluoride concentration increases. The last semi-circle is terminated by an inductive loop at low frequencies that very definitely signifies the presence of adsorbed species.

3.2.3. Spectra obtained with chloride and fluoride present

3.2.3.1. Potential effects. The impedance diagrams in Fig. 16 were obtained at constant Cl^- and F^- (5×10^{-2} mol dm^{-3}) concentrations and pH 1.7 but at different potentials in the localized corrosion region corresponding to each side of the anodic peak (Fig. 8c). Two capacitive semi-circles are seen at 0.03 V/SCE (spectrum 1). These semi-circles are characteristic of reactions in a porous oxide layer and an oxide sublayer [32] as shown in Fig. 17. At the potentials corresponding to the maximum height and negative slope in the anodic peak, only a capacitive semi-circle (spectra 2 and 3) is observed at high frequencies, then the capacitive branch tends towards a high imaginary impedance value at medium frequencies, and at low frequencies, this bends to negative real impedance values. In spectrum 4 obtained at 0.1 V/SCE, a capacitive semi-circle is seen at high frequencies. The semi-circle diameter increased with respect to the preceding diagrams (spectra 1 to 3) definitely signifying corrosion product accumulation partially protecting Inconel 600. This semi-circle is followed by a straight line at low frequencies. It may be a Warburg straight line corresponding to diffusion in oxide, but its slope is slightly different ($\sim 45°$), and also, for these experimental conditions, the passive oxide layer does not form. The straight line would appear to signify an anodic reaction accompanied by ionic diffusion through the oxide layer as suggested by SEM examinations (Fig. 11).

3.2.3.2. Fluoride and pH effects. The impedance diagrams in Fig. 18 were obtained at constant potential (0.07 V/SCE) and Cl^- (5×10^{-2} mol dm^{-3}), but at different

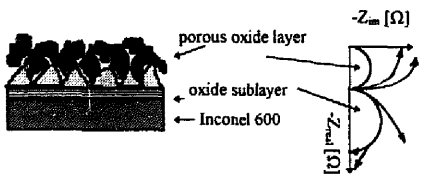

Fig. 17. Schematic view of oxide layer system and corresponding impedance diagram in the complex plane.

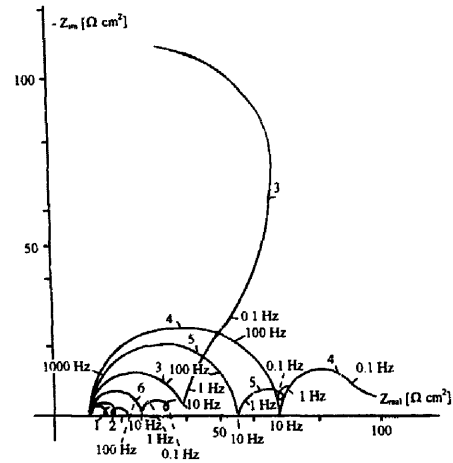

Fig. 18. Impedance diagrams of Inconel 600 surface area: 0.2 cm^2, temperature: 20°C, *E*: 0.07 V/SCE, ω: 2000 rpm, Cl^-: 5×10^{-2} mol dm^{-3}, effect of F^- and pH: (1): F^-: 10^{-2} mol dm^{-3}, pH: 1, (2): F^-: 2×10^{-2} mol dm^{-3}, pH: 1.2, (3): F^-: 5×10^{-2} mol dm^{-3}, pH: 1.7, (4): F^-: $7\ 10^{-2}$ mol dm^{-3}, pH: 2.1, (5): F^-: 0.1 mol dm^{-3}, pH: 3.5, (6): F^-: 0.12 mol dm^{-3}, pH: 3.6.

F^- concentrations and pH in the localized corrosion region corresponding to the anodic peak (Fig. 8(c)). The impedance diagrams obtained with 10^{-2} and 2×10^{-2} mol dm^{-3} F^- are shown in spectra 1 and 2. Two capacitive semi-circles at high and low frequencies separated by a loop are observed. Their origin is likely to be the same as that for Figs. 12 and 13. The impedance diagrams are different for 5 and 7×10^{-2} mol dm^{-3} F^- (spectra 3 and 4). For spectrum 3, the capacitive branch tends rapidly to high imaginary impedance values at low frequencies. Finally, for still lower frequencies, this approaches negative real impedance values. According to Laihonen et al. [32], Rouquette-Sanchez et al. [33] and Keddam [34], these diagrams would result from adsorption, reactions with diffusion through oxide layer, active dissolution and dissolution with localized corrosion. For a fluoride concentration of 7×10^{-2} mol dm^{-3} (spectrum 4), the impedance diagram consists of two capacitive semi-circles; the second semi-circle lies along the real impedance axis at the low frequencies. Finally, for spectra 5 and 6, obtained at 0.1 and 0.12 mol dm^{-3} F^-, the second capacitive semi-circle is terminated at low frequencies by an inductive loop. In spectra 1 to 4, the semi-circle size increases at high frequencies whereas in spectra 4 to 6, it decreases when the fluoride concentration increases. These different diagrams show the dependence of modifications of Inconel

600 behavior on the fluoride concentration. Depending on the pH and oxide layer, the localized corrosion by Cl^- and F^- ions must slightly decrease or increase as noted previously in the anodic peak region (Fig. 8).

4. Discussion, equivalent circuits and value determination

4.1. Discussions

These experimental diagrams can be interpreted following the explanations given by Keddam [34], Epelboin et al. [35] and Jouanneau and Keddam [36]. Equivalent circuit models were proposed by Epelboin [35] and by Chu-Nan Cao [37,38]. In the interpretation, the current (i) is a function of the chosen potentials in the anodic peak and a parameter (x) depending on adsorbed species and oxide layer [32]:

$$i = f(E, x). \tag{10}$$

With adsorbed species, the faradaic impedance is

$$1/Z_F = 1/R_{ct} + f'_E b/(j\omega - a), \tag{11}$$

where $f'_E = (\partial i/\partial E)_x$ is the ratio of the current to potential variations, R_{ct} the charge transfer resistance, ω angular frequency and a and b are dependent on

$$a = \left(\partial(\mathrm{d}x/\mathrm{d}t)/\partial x\right)_E = \tau_x^{-1}, \tag{12}$$

$$b = \left(\partial(\mathrm{d}x/\mathrm{d}t)/\partial E\right)_x, \tag{13}$$

where τ_x is the time constant for a given value of x. From these equations, for a sufficiently high frequency with $\omega \gg \tau_x^{-1}$, the expression $f'_E b/(j\omega - a)$ tends to zero, and we have

$$(1/Z_F)_{f\to\infty} = 1/R_{ct}. \tag{14}$$

At very low frequencies, with $\omega \ll \tau_x^{-1}$ the current varies with the potential, and we obtain

$$(1/Z_F)_{f\to 0} = 1/R_{ct} - 1/\varphi = 1/R_p, \tag{15}$$

where R_p is the polarization resistance and $1/\varphi$ depends on $f'_E b/a$. At the high-frequency limit, the impedance is equal to the electrolyte resistance. At the low-frequency limit, the faradaic impedance, i.e., R_p, can be considered equal to the slope of the polarization curve ($\partial i/\partial E$) at the steady state.

From the previous equations (Eqs. (10) and (13)), the adsorbed species also play a role in these spectra. For this, Jouanneau and Keddam [36] showed that the OH^- ions adsorb on metal forming a Me–OH dipole allowing electron transfer at the reactive interface. According to these authors, the oxide layer would provide adsorbed OH^- ions. For another adsorbed species, e.g., X^- anion which could be F^- or Cl^-, there is competitive adsorption with OH^- ions, and this can lead to oxide layer modification, depassivation, active dissolution and dissolution with localized corrosion. On the basis of the interpretation given by Jouanneau and Keddam [36], a reaction scheme can be written for competitive adsorption, oxide layer modification and depassivation:

(16)

In this scheme, 'of' is the oxide layer formation, 'om' the oxide layer characteristic modification, 'pd' the primary depassivation and 'sd' the secondary depassivation leading to the dissolution reaction (disso.) of Inconel 600 by active and localized corrosion. This reaction scheme would involve several steps beginning with adsorption, and where pH, oxide layer and potential may also have an effect.

4.2. Spectra obtained with chloride present

The general simplified equation (according to, for example, Bessone et al. [39]) corresponding to an oxide layer is

$$Z = R_{el} + \left(jC_{dl}\omega + Z_F^{-1}\right)^{-1}, \tag{17}$$

where C_{dl} represents the double layer capacitance, R_{el} the electrolyte resistance, $\omega = 2\pi f$, f being frequency, and Z_F the faradaic impedance including several electrical components. In Fig. 19(a), the faradaic impedance consists of charge transfer resistances (R_n) with a small diffusion term, an inductance (L) depending on bf'_E, and finally the resistive term, φ, in addition to the inductance. The resistive term, φ, will have little effect on simulated diagrams. According to these, the faradaic impedance is

$$Z_F = R_1 + \frac{j\omega LR_2}{R_2 + j\omega L}. \tag{18}$$

The simulated spectra corresponding to Figs. 12 and 13 are shown in Figs. 20 and 21. The frequency of the top of the first capacitive semi-circle increases with a higher Cl^- concentration (e.g., curves 1 and 2 in Fig. 21) and depends on pH. The size, shape of semi-circles or loop, and position of the frequencies coincide with the experimental diagrams, and thus allow the determination of parameters from the Circelec software program written by Diard et al. [11,12]. The values of the main equivalent circuit elements are given in Tables 3 and 4. As the potentials or Cl^- concentration increase, the values of resistances decrease; this is the result of the corrosion increasing. Also, according to Fig. 14, the corrosion is lower at higher pH.

4.3. Spectra obtained with fluoride present

The curves obtained with different fluoride concentrations and for 0.05 V/SCE (Fig. 15) can be satisfactorily explained on the basis of the same equivalent circuit

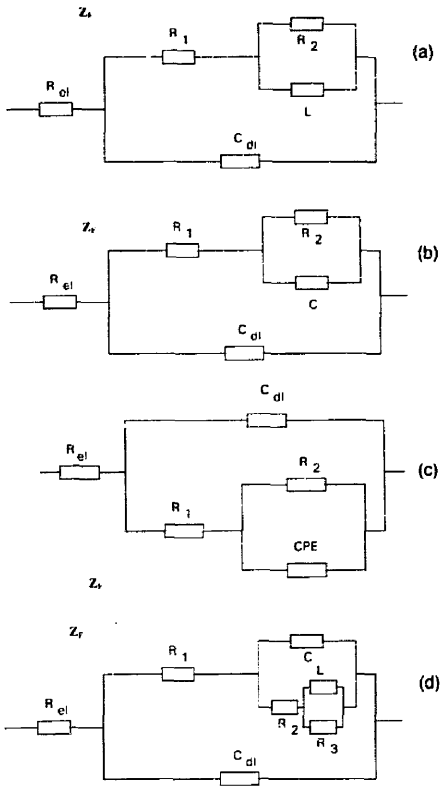

Fig. 19. Equivalent circuits for impedance simulation (a) following Fig. 11Fig. 12Fig. 16, curve: 1, Fig. 18, curves: 1 and 2. R_{el} and R_n: electrolytic and charge transfer resistances, C_{dl}: double layer capacitance, L: inductance, (b) following Fig. 16, curves 2 and 3, Fig. 18, curves 3 and 4, R_{el} and R_n: electrolytic and charge transfer resistances, C_{dl} and C: double layer capacitance and capacitance, (c) following Fig. 16, curve 4, R_{el} and R_n: electrolytic, charge transfer resistances, C_{dl}: double layer capacitance, CPE: constant phase element, (d) following Fig. 18, curves 5 and 6, R_{el} and R_n: electrolytic, charge transfer resistances, C_{dl}: double layer capacitance, L: inductance.

approach presented in Fig. 19(a). From these, the simulated spectra (Fig. 22) have two capacitive semi-circles and an inductive loop at low frequencies. The mean error in spectra is less than 5%. There is therefore very good agreement between the experimental and fitted data. The values of the equivalent circuit elements are given in Table 5. The charge transfer resistance decreases at higher fluoride concentration: this is the result of corrosion increasing. From the general equations giving the relation be-

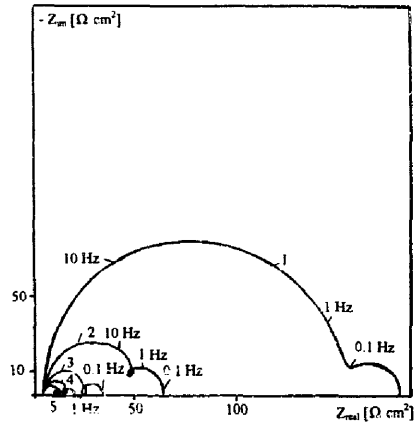

Fig. 20. Simulated impedance diagrams for comparison with Fig. 12, Cl^-: 5×10^{-2} mol dm^{-3}, potential effect: (1): 0, (2): 0.025, (3): 0.065, (4): 0.08, (5): 0.1 V/SCE, parameter values in Table 3.

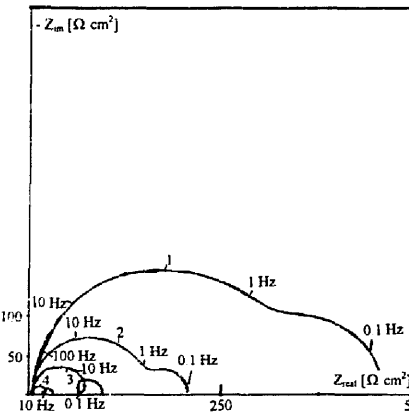

Fig. 21. Simulated impedance diagrams for comparison with Fig. 13, E: 0.05 V/SCE, effect of Cl^-: (1): 5×10^{-3}, (2): 10^{-2} mol dm^{-3}, (3): 2×10^{-2} mol dm^{-3}, (4): 5×10^{-2} mol dm^{-3}, parameter values in Table 4.

Table 3
Effect of potential for 5×10^{-2} mol/dm^3 Cl^-

	E/V/SCE					
	0	0.025	0.05	0.065	0.08	0.1
R_{el} (Ω cm^2)	8	7	7	6.5	6	6
R_1 (Ω cm^2)	140	60	12	21	11	6
R_2 (Ω cm^2)	90	17	7	9	7	6
C/(μF cm^{-2})	250	200	120	160	160	160

Table 4
Effect of Cl^- at 0.05 V/SCE

$Cl^- \times 10^{-2}$ mol/dm^3	0.5	1	2	5
R_{ct} (Ω cm^2)	10	8	6	4
R_1 (Ω cm^2)	300	140	20	9
R_2 (Ω cm^2)	250	90	45	7
C/ (μF cm^{-2})	150	150	50	120

Table 5
Effect of F^- at 0.05 V/SCE

$F^- \times 10^{-2}$ mol/dm^3	1	6	8	10
R_{ct} /Ω cm^2)	10	7	5.5	4
R_1 (Ω cm^2)	15	11	7	5
R_2 (Ω cm^2)	60	45	41	39
C/ (μF cm^{-2})	10	25	30	40

tween the diffusion coefficient and the diffusion thickness [40] and the experimental results obtained by the Circelec program [11], the expression for the diffusion coefficient is

$$D/\delta^2 = 0.1, \tag{19}$$

where δ is the diffusion layer thickness. If we take the previous value of D, the thickness is a few μm.

4.4. Spectra obtained with chloride and fluoride present

4.4.1. Potential effects

As indicated by Al-Kharafi and Badawy [41], the main advantage of electrochemical impedance spectroscopy is the use of an electronic model to represent the metal–electrolyte interface. An interface undergoing electrochemical reactions is typically analogous to an electronic circuit consisting of a specific combination of resistors, capacitors and inductors, and hence an electrochemical system can be characterized in terms of its equivalent circuit. For a given electrochemical system, impedance plots can be correlated with one or more equivalent circuits. The correlation is used to verify models for the system. Once a particular model is chosen, physical and/or chemical properties can be correlated with circuit elements and numerical values are obtained by fitting experimental data to the equivalent circuit. Simple equivalent circuits generate relatively straightforward results to present metal–oxide–electrolyte systems. It is essential to subject equivalent circuit models, that are found to represent a good approach to electrochemical systems to obtain reasonable matching of data.

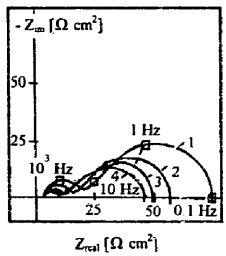

Fig. 22. Simulated impedance diagrams for comparison with Fig. 15. E: 0.05 V/SCE, effect of F^-: (1): 10^{-2}, pH 1, (2): 6×10^{-2}, pH 1.9, (3): 8×10^{-2}, pH 2.3, (4) 10^{-1} mol dm^{-3}, pH 3.5, parameter values in Table 5.

The experimental diagrams (Fig. 16), obtained at different potentials in the anodic peak and with constant Cl^- and F^- concentrations and pH 1.7, can be satisfactorily explained on the basis of equivalent circuits (Fig. 19(a)–(c)) according to the explanations given by Epelboin et al. [35] and Jouanneau and Keddam [36]. In Fig. 19(b), the faradaic impedance implies resistances and a capacitance linked to $a\tau_1/bR_1^2f_F'$. From this, the faradaic impedance is given in Eq. (20):

$$Z_F = R_1 + \frac{R_2}{1 + j\omega R_2 C} \tag{20}$$

where R_1 is R_{ct} in Eq. (11) and R_2 represents $R_{ct}^2/[(a/bf_F') - R_{ct}]$. The simulated spectra proposed in Fig. 23 are compared to those obtained experimentally in Fig. 16. The simulated spectrum 1 corresponds to resistances and an inductance (L) in the equivalent circuit (Fig. 19(a)). Spectra 2 and 3 correspond to a resistance in parallel with a capacitance (Fig. 19(b)). Spectrum 4 shows a capacitive semi-circle followed by a straight line at low frequencies. The straight line is a depressed semi-circle with a very long time constant represented by a constant phase element (CPE). It is due to a partial ionic transfer and indicates a reaction in a porous and duplex layer that does not guarantee good corrosion protection. The diffusion of the dissolving species through the layer limits the corrosion rate. The equivalent circuit (Fig. 19(c)) corresponds to the double layer capacitance, charge transfer resistances, and constant phase element defined as

$$Z_{CPE} = B(j2\pi f)^{-a} \tag{21}$$

in which a is a slope between 0 and 1, $j = \sqrt{-1}$, and B is a frequency-independent constant considered as the reciprocal capacitance only if $a \approx 1$.

Table 6
Effect of potential for 5×10^{-2} mol dm^{-3} Cl^- and 5×10^{-2} mol/dm^3 F^-

E/V/SCE	0.03	0.05	0.07	0.1
R_{ct} (Ω cm^2)	7	9	9	10
R_1 (Ω cm^2)	15	40	40	120
C_{dl} (μF cm^{-2})	50	25	30	45
τ (s)	8	5	10	–
Z_{CPE}	–	–	–	0.02
a	–	–	–	0.6

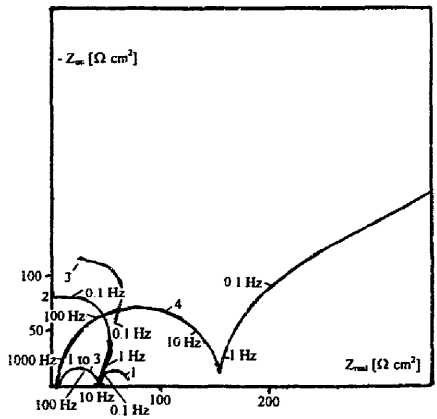

Fig. 23. Simulated impedance diagrams for comparison with Fig. 16. Cl^-: 5×10^{-2} mol dm^{-3}, F^-: 5×10^{-2} mol dm^{-3}, pH 1.7, potential effect: (1): 0.03, (2): 0.05, (3): 0.07, (4): 0.1 V/SCE, parameter values in Table 6.

These different diagrams show the complexity of the system studied and the change in the equivalent circuit with potential. One of the aims of plotting the diagrams was to find the values of the main electrical elements and, if possible, to interpret them as a function of potentials. These are given in Table 6: the value of the double layer capacitance corresponds to a normal value according to Bard and Faulkner [40]. Its variation signifies lower corrosion and then corrosion enhancement. The charge transfer resistance is small and slightly increases with the potentials signifying then a very slight oxide layer improvement. From the simulated diagrams obtained by the Circelec software programs and according to Eqs. (10)–(15), the lowest frequency branch which bends towards the negative real impedance value corresponds to the negative $\partial i/\partial E$ slope obtained at point C in voltammetry (Fig. 8(a), (c)); this appears to agree with the theoretical interpretation proposed by Keddam [34] and Epelboin et al. [35] for a negative polarization resistance.

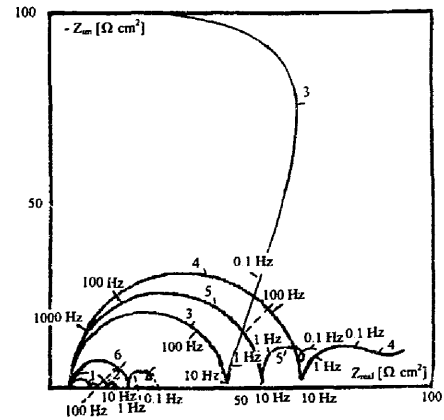

Fig. 24. Simulated impedance diagrams for comparison with Fig. 18. Cl^-: 5×10^{-2} mol dm^{-3}, E: 0.07 V/SCE, effect of F^- and pH. (1): F^-: 10^{-2} mol dm^{-3}, pH: 1, (2): F^-: 2×10^{-2} mol dm^{-3}, pH: 1.2, (3): F^-: 5×10^{-2} mol dm^{-3}, pH: 1.7, (4): F^-: 7×10^{-2} mol dm^{-3}, pH: 2.1, (5): F^-: 0.1 mol dm^{-3}, pH: 3.5, (6): F^-: 0.12 mol dm^{-3}, pH: 3.6, parameter values in Table 7.

Table 7
Effect of fluoride concentration, for 5×10^{-2} mol dm^{-3} Cl^-, at 0.07 V/SCE

$F^-\times10^{-1}$ mol dm^{-3}	0.1	0.2	0.5	0.7	1	1.2
pH	1	1.2	1.7	2.1	3.5	3.6
R_{el} (Ω cm^2)	7	8	10	9	8	7
R_1 (Ω cm^2)	8	3	20	60	50	15
C_{dl} (μF cm^{-2})	100	70	10	10	20	50

4.4.2. Medium effects

The experimental diagrams (Fig. 18) obtained in presence of Cl^- and at different F^- concentrations and pH can be satisfactorily explained on the basis of equivalent circuits (Fig. 19(a), (b) and (d)). From these circuits, we drew the simulated diagrams (Fig. 24) which coincide exactly with the experimental diagrams to ascertain the suitable electrical elements using the Circelec software program.

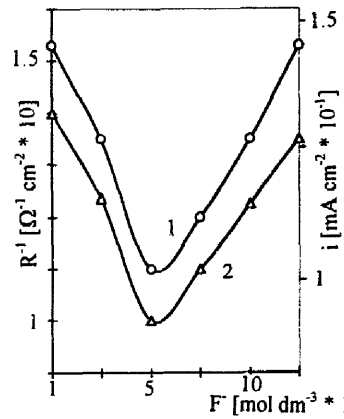

Fig. 25. i and R_1^{-1} versus F^- from Fig. 8(a), (c) and Table 7. (1): impedance Ω^{-1} cm^{-2}, (2): current mA cm^{-2}.

The values of the equivalent circuit elements are given in Table 7. It can be seen that the charge transfer resistance (R_1) increases then decreases when F^- concentration and pH increase. It can be also seen that the value of the double layer capacitance varies inversely. Fig. 25 presents the variation of R_1^{-1} and i versus fluoride concentration from impedance and voltammetry measurements (Fig. 8a, c). As shown in this figure, the values R_1^{-1} and i decrease at lower F^- concentration, and then these increase starting with the same F^- concentration. This mean that the rate of oxide layer corrosion changes as predicted with the F^- concentration and pH ($\approx 5 \times 10^{-2}$ mol dm^{-3}). This change indicates that pH, adsorbates, F^-, Cl^- concentrations modify the nature of oxide layer and corrosion mode in overlapping active and pitting regions.

5. Conclusions

It is possible to interpret the cyclic voltammetry and electrochemical impedance spectroscopy results for the active and localized corrosion overlapped regions of Inconel 600 subjected to tritiated water containing chloride in which fluoride concentration and acid pH vary. The polarization curves show a well defined localized corrosion region over a wide range of potentials going from the corrosion potential up to the transpassivity. Two influences are then observed in the overlapped regions during the pH increase: the first gives a slight decrease in corrosion, for the second, the F^- and Cl^- concentrations must be high enough to produce more corrosion. It can be thought also that the adsorbed species such as OH^-, Cl^-, F^- lead to active and localized corrosion. The interpretation of the impedance diagrams was made by proposing several equivalent circuits where the main electrical component values are determined. The characteristics of the oxide layer were found to depend not only on the nature of the electrolyte but also on its concentration. The oxide layer should therefore have a complex structure, this is shown by equivalent circuit elements which depend on the adsorbed species. In addition to important conclusions concerning the influence of chloride and fluoride in highly radioactive aqueous environments on localized corrosion, the work described here is an advantageous approach to the problem of localized corrosion based on purely electrochemical methods.

References

[1] G. Bellanger and J.J. Rameau, Corros. Sci. 36 (1994) 545.
[2] G. Bellanger, J. Nucl. Mater. 210 (1994) 63.
[3] A. Roustila, N. Kuromoto, A.M. Brass and J. Chêne, J. Nucl. Mater. 211 (1994) 156.
[4] A.M. Brass, J. Chêne and J. Gonzales, Metal. Mater. Trans. 25A (1994) 1159.
[5] G. Bellanger, Fusion Technology, J. Am. Nucl. Soc. 27 (1995) 46.
[6] G. Bellanger and J.J. Rameau, Fusion Technology, J. Am. Nucl. Soc. 24 (1993) 145.
[7] A. Bruggeman, M. Snykers and P. de Regge, Fusion Technology, J. Am. Nucl. Soc. 14 (1988) 828.
[8] W.G. Burns and P.B. Moore, Radiat. Eff. 30 (1976) 233.
[9] J.K. Linacre and W.R. Marsh, Report R 10027, (Chemistry Division, Atomic Energy Research Establishment, Harwell, 1981).
[10] J. Wright, J.K. Linacre, W.R. Marsh and T.R. Bates, in: Proc. Int. Conf. on the Peaceful Uses of Atomic Energy, 1955, Vol. 7 (United Nations, New York, 1956) p. 560.
[11] J.P. Diard, P. Landaud, B. Le Gorrec and C. Montella, Deuxième Forum sur les Impedances Electrochimiques, Montrouge, 1987, ed. C. Gabrielli (Université P. et M. Curie, Paris).
[12] J.P. Diard, B. Le Gorrec and S. Maximovitch, Electrochim. Acta 35 (1990) 1099.
[13] M. Rouby, Les Aciers Inoxydables, eds. P. Lacombe et al. (Physique, Les Ulis, France, 1990) p. 915.
[14] P. Houlle, in: Corrosion Localisée, eds. F. Dabosi et al. (Physique, Les Ulis, France 1994) p. 621.
[15] F. Dupoiron and M. Vernon, in: Corrosion Localisée, eds. F. Dabosi et al. (Physique, Les Ulis, France, 1994) p. 605.
[16] J.W. Schultze and V.A. Maragno, Electrochim. Acta 31 (1986) 355.
[17] C. Kerrec, D. Devilliers, C. Hinnen and P. Marcus, in: Symp. Modifications of Passive Films, 1993, eds. P. Marcus et al. (European Federation of Corrosion, London, 1994) p. 206.
[18] G. Bellanger, Fusion Technology, J. Am. Nucl. Soc. 27 (1995) 36.
[19] P.E. Morris and R.C. Scarberry, Corrosion 26 (1970) 169.
[20] G. Bellanger and J.J. Rameau, J. Nucl. Mater. 24 (1996) 228.
[21] A. Wieckowski, E. Ghali and Huy Ha Le, J. Electrochem. Soc. 131 (1984) 9.
[22] J. Chêne, A.M. Brass and F.P Ford, in: Stress Corrosion, Phenomenology and Mechanisms, eds. Desjardins and Oltra (Physique, Les Ulis, France, 1992) p. 159–210, 833–864.
[23] A. Sehgal, B.G. Ateya and H.W. Pickering, J. Electrochem. Soc. 142 (10) (1995) 198.
[24] R.G. Ballinger, R.M. Latanision, W.C. Moshier and K.N. Siebein, in: Proc. Int. Congr. on Metallic Corrosion, Toronto, 1984, ed. H.P. Godard, Vol. 1 (National Research Council of Canada, Ottawa, 1984) p. 265.
[25] G. Pinard-Legry, H. Coriou, L. Grall and A. Besnard, in: Proc. 1er Conf. Int. Hydrogène dans les Métaux, Paris, 1972, ed. P. Bastien, Vol. 1 (Science et Industrie, Paris, 1972) p. 241.
[26] A.M. Farvaque-Béra and S. Leistikow, J. Nucl. Mater. 185 (1991) 1.
[27] P. Delahay, New Instrumental Methods in Electrochemistry (Interscience, New York, 1954).
[28] T.E. Pou, O.J. Murphy, V. Young and J. O'M Bockris, in: Proc. Int. Congr. on Metallic Corrosion, Toronto, 1984, ed. H.P. Godard, Vol. 2 (Conseil National de Recherches du Canada, Ottawa, 1984) p. 141.
[29] T.P. Moffat and R.M. Latanision, J. Electrochem. Soc. 139 (1992) 7.
[30] H.W. Pickering, Mater. Sci. Eng. A198 (1995) 213.

[31] K. Cho and H.W. Pickering, J. Electrochem. Soc. 138 (1991) 10.
[32] S. Laihonen, T. Laitinen, G. Sundholm and A. Yli-Pentti, Electrochim. Acta 35 (1) (1990) 229.
[33] S. Rouquette-Sanchez, P. Cowache P. Boncorps and J. Vedel, Electrochim. Acta 38 (1993) 2043.
[34] M. Keddam, in: Corrosion Mechanisms in Theory and Practice, eds. P. Marcus and J. Oudar (Marcel Dekker, New York, 1995) p. 55.
[35] I. Epelboin, C. Gabrielli, M. Keddam and H. Takenouti, in: Comprehensive Treatise of Electrochemistry, Vol. 4, Electrochemical Materials Science, eds. J. O'M Bockris et al. (Plenum, New York, 1981) p. 151.
[36] A. Jouanneau, M. Keddam and M.C. Petit, Electrochim. Acta 21 (1976) 287.
[37] Chu-Nan Cao, Electrochim. Acta 35 (5) (1990) 831.
[38] Chu-Nan Cao, Electrochim. Acta 35 (5) (1990) 837.
[39] J.B. Bessone, D.R. Salinas, C.E. Mayer, M. Ebert and W.J. Lorenz, Electrochim. Acta 37 (1990) 2283.
[40] A.J. Bard and L.R. Faulkner, Electrochemical Methods. Fundamentals and Applications (Wiley, New York, 1980).
[41] F.M. Al-Kharafi and W.A. Badawy, Electrochim. Acta 40 (16) (1995) 2623.